Journal of Structural Geology 31 (2009) 328–345

Contents lists available at ScienceDirect

Journal of Structural Geology

journal homepage: www.elsevier.com/locate/jsg

Structural geology and 4D evolution of a half-graben: New digital outcrop modelling techniques applied to the Nukhul half-graben, Suez rift, Egypt

Paul Wilson [a,*], David Hodgetts [a], Franklin Rarity [a], Rob L. Gawthorpe [a], Ian R. Sharp [b]

[a] Basin Studies and Petroleum Geoscience, School of Earth, Atmospheric and Environmental Sciences, University of Manchester, Williamson Building, Oxford Road, Manchester M13 9PL, United Kingdom
[b] StatoilHydro Research Centre, Sandsliveien 90, Bergen, Norway

ARTICLE INFO

Article history:
Received 16 June 2008
Received in revised form
3 November 2008
Accepted 17 November 2008
Available online 10 December 2008

Keywords:
Normal faults
Fault growth
Fault linkage
Rift basins
Suez rift

ABSTRACT

LIDAR-based digital outcrop mapping, in conjunction with a new surface modelling approach specifically designed to deal with outcrop datasets, is used to examine the evolution of a half-graben scale normal fault array in the Suez rift. Syn-rift deposition in the Nukhul half-graben was controlled by the graben-bounding Nukhul fault. The fault can be divided into four segments based on the strike of the fault, the morphology of hangingwall strata, and the variation in throw along strike. The segments of the fault became geometrically linked within the first 2.5 m.y. of rifting, as evidenced by the presence of early syn-rift Abu Zenima Formation strata at the segment linkage points. Fault-perpendicular folds in the hangingwall related to along-strike variations in throw associated with precursor fault segments persist for a further 1.8 m.y. after linkage of the segments, suggesting that the fault remains kinematically segmented. We suggest this occurs because of sudden changes in fault strike at the segment linkage points that inhibit earthquake rupture propagation, or because displacement is geometrically inhibited at fault linkage points where the orientation of the intersection line of the segments is significantly different from the orientation of the slip vector on the fault system. Length/throw plots and throw contour patterns for minor faults show that some faults initiated in pre-rift strata, whereas late east-striking faults initiated in the syn-rift basin fill. The late initiating faults are spatially associated with the east-striking Baba–Markha fault, which was active throughout the rift history, but developed as a transfer fault between major block-bounding fault systems around 6–7 Ma after rift initiation.

1. Introduction

The growth, interaction and linkage of normal fault systems through time are critical factors to the understanding of syn-rift sediment dispersal and stratigraphic development (e.g. Gawthorpe and Leeder, 2000). Models of normal fault growth and linkage fall into two types. In the first type, fault length increases as faults propagate laterally, and initially isolated faults link with other faults along strike to create longer faults (e.g. Cartwright et al., 1995; Cowie et al., 2000; Gawthorpe et al., 2003). In this case, much of the history of the fault is characterised by displacement on independent segments (Fig. 1a). In the second type, particularly applicable to reactivated faults, the fault length is established early in its history, leading to displacement accruing on a fault that has an approximately constant length for much of its lifetime (e.g. Nicol et al., 2005; Bull et al., 2006; Manzocchi et al., 2006; Fig. 1b). Patterns of fault growth and linkage are likely to be complicated where pre-existing basement fabrics and structures exert an influence on syn-rift structural development (Montenat et al., 1988; Morley, 1999; Younes and McClay, 2002; Bellahsen and Daniel, 2005). We test this proposition in the Suez rift, in which three sets of inherited basement structures have been identified as contributing to rift development: (i) a 'clysmic' trend striking approximately 140°, parallel to the major rift-bounding faults; (ii) an 'Aqaba' trend striking approximately 000–020°; and (iii) a 'Duwi' trend striking approximately 100–120° (Montenat et al., 1988; Younes and McClay, 2002; Bosworth et al., 2005).

Previous studies of normal fault evolution have generally focused on interpretation of subsurface datasets, particularly 3D seismic, (e.g. Contreras et al., 2000; McLeod et al., 2000; Corfield and Sharp, 2000; Young et al., 2000; Morley, 2002; Nicol et al., 2005; Bull et al., 2006), or outcrop study (e.g. Sharp et al., 2000a,b; Jackson et al., 2002; Gawthorpe et al., 2003). These studies tend to focus either on single faults (e.g. Nicol et al., 2005) or relatively simple fault systems consisting of a few fault segments (e.g. Sharp

* Corresponding author.
E-mail address: paul.wilson@manchester.ac.uk (P. Wilson).

0191-8141/$ – see front matter © 2008 Elsevier Ltd. All rights reserved.
doi:10.1016/j.jsg.2008.11.013

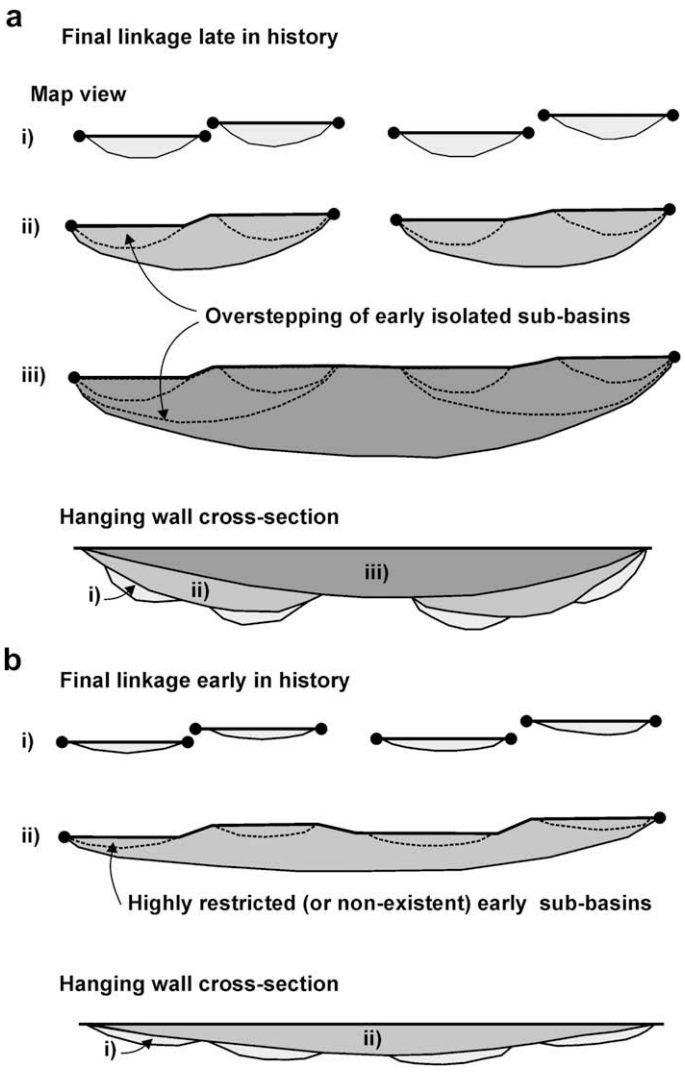

Fig. 1. Models of fault linkage and growth. (a) Final linkage of the fault system occurs late in its history. In this case much of the history of the fault is characterised by displacement on independent fault segments. (b) Final linkage of the fault system occurs early in its history. The length of the fault system is established early, and the history of the system is characterised by increasing displacement with little or no increase in fault length. Modified after Morley et al. (2007).

et al., 2000a). Seismic-based studies have excellent 3D coverage, but suffer from low vertical resolution (of the order of 20–40 m). Outcrop studies have much greater resolution, but generally suffer from a lack of 3D coverage and difficulties in collecting quantitative data. The challenge is to combine data that is 3D, accurate and quantitative with the high resolution available from outcrop study. Here we utilise a half-graben scale terrestrial LIDAR dataset (Bellian et al., 2005; Pringle et al., 2006; Redfern et al., 2007) of a normal fault array in the Suez rift and its associated syn-rift stratigraphy. Lack of vegetation and deeply incised wadi systems in the study area give exceptional pseudo-3D exposure. A new surface modelling approach, designed specifically for outcrop datasets that typically have areas of high data density and areas of low to non-existent data density, is used to model the geometry of key geological horizons within the half-graben. These surfaces can be exported to commercially available geological modelling software (Schlumberger's Petrel suite and Badley Geoscience Ltd.'s Trap-Tester). We use the resulting models to create structure contour maps of geological horizons, and displacement-length plots and throw maps of the faults within the array, thereby constraining the processes of growth and linkage within the array.

2. Geological setting

The Suez Rift is the northwestern extension of the Red Sea rift. It developed in Oligo-Miocene time as a result of the separation of the Arabian and African plates (e.g. Garfunkel and Bartov, 1977; Lyberis, 1988; Patton et al., 1994). The rift is approximately 300 km long and up to 80 km wide and is bounded by normal faults defining half-graben style tilted fault blocks. The rift has been divided into three dip provinces characterised by their differing fault polarity: the northern and southern dip provinces where normal faults dip dominantly to the northeast and strata dip dominantly to the southwest; and the central dip province, where normal faults dip dominantly to the southwest and strata dip dominantly to the northeast (Moustafa, 1993). The dip provinces are separated from each other by rift-transverse accommodation zones (Moustafa, 1996, 1997). The Hammam Faraun fault block (Fig. 2), in which the present study area is located, forms part of the central dip province.

The Hammam Faraun fault block has a half-graben geometry, with strata dipping gently to the northeast. It is bounded to the east by the Thal fault (displacement ~ 1850 m), to the west by the Hammam Faraun fault (displacement ~ 4800 m) and to

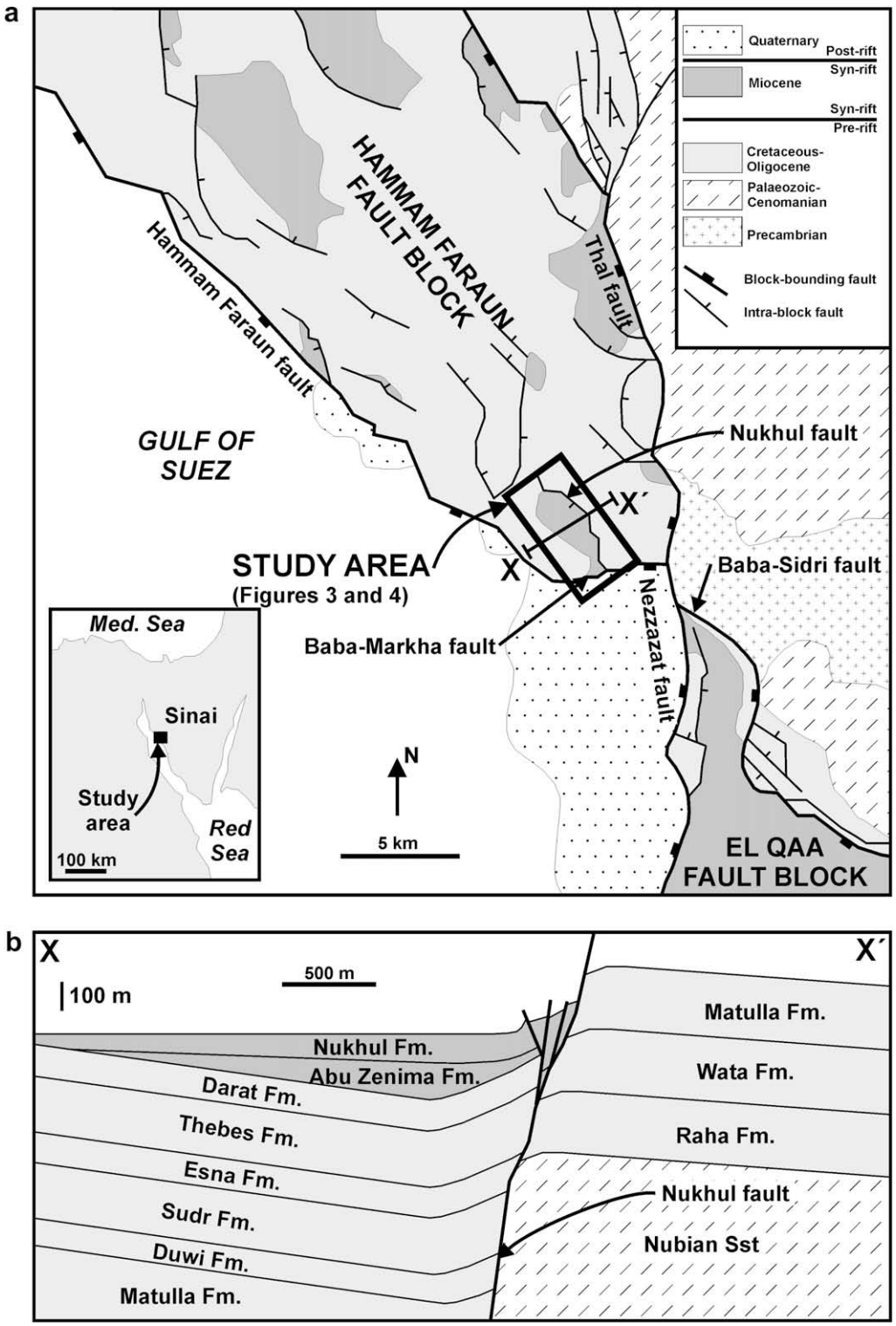

Fig. 2. Geological setting of the Nukhul half-graben. (a) Simplified map of the Hammam Faraun and El-Qaa fault blocks, showing block-bounding and major intra-block faults. (b) Cross-section of the Nukhul half-graben along section *X*–*X*′ in (a). Modified after Sharp et al. (2000a) and Jackson et al. (2006).

the south by the Baba–Markha fault (displacement ~ 3500 m) (Fig. 2; Moustafa, 1993). These major block-bounding normal faults are in excess of 25 km long and dip steeply (60–80°) to the west (e.g. Moustafa, 1993). The fault block contains numerous subordinate intra-block faults, some of which are associated with areas of preserved syn-rift stratigraphy (Fig. 2). One of these areas is the Nukhul half-graben, bounded to the northeast by the intra-block Nukhul fault and to the south by the block-bounding Baba–Markha fault (Figs. 2–4), and which is the field area for this study.

The Nukhul half-graben is cut by a fault array consisting of three orientation sets (stereonet on Fig. 4); an approximately northwest-striking set, an approximately north-striking set, and an

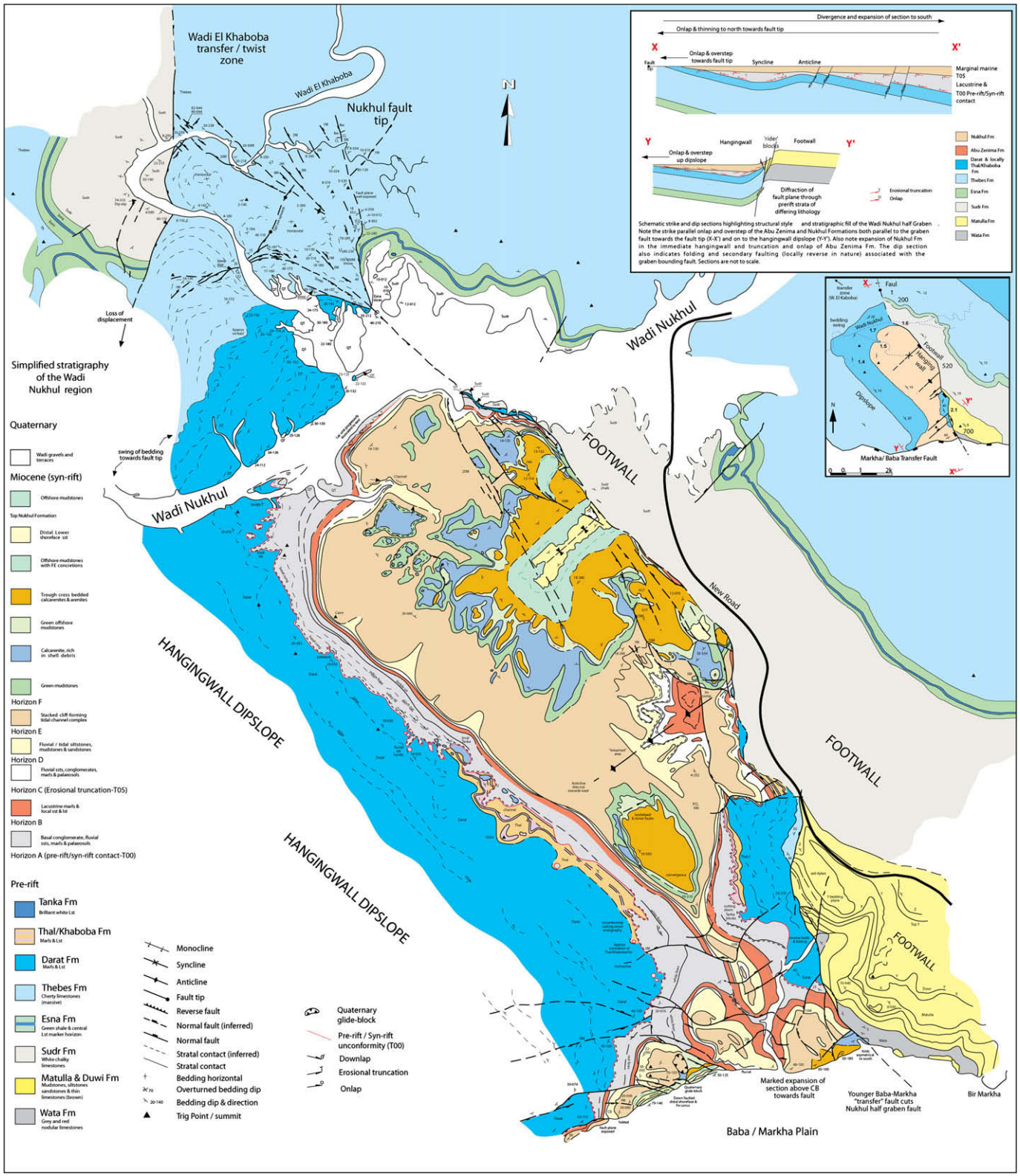

Fig. 3. Detailed geological map of the Nukhul half-graben.

approximately east-striking set. These fault sets correspond to the orientations of reactivated basement structures in the Gulf of Suez identified by previous workers (clysmic, Aqaba and Duwi trends: Montenat et al., 1988; Younes and McClay, 2002). Normal faults antithetic to the main Nukhul fault, typically 1–2 km in length, are developed in the Nukhul fault hangingwall (Figs. 3 and 4). Antithetic faults are sub-parallel to the main Nukhul fault, consisting of NW-SE and N-S striking segments (Figs. 3 and 4). East-striking faults include the block-bounding Baba–Markha fault and are spatially restricted to the southern part of the study area (Figs. 3 and 4). The Baba–Markha fault has a zig-zag morphology in plan view, being composed of segments that trend approximately 065° and 090°. Faults in the array are generally steep (dip >50°), with some exceptions where faults have been passively rotated into low-angle orientations during fault-propagation folding adjacent to major faults (Sharp et al., 2000a,b; Wilson et al., submitted for publication).

3. Stratigraphic framework

Pre-rift strata in the study area comprise two megasequences (Robson, 1971; Moustafa, 1987; Sharp et al., 2000a; Jackson et al., 2006). Megasequence 1 consists of Nubian sandstone (Cambrian to Lower Cretaceous in age) that unconformably overlies Precambrian 'pan-African' basement. Megasequence 2 consists of a Cretaceous mixed carbonate-clastic succession (Raha, Wata, Matulla, Duwi and Sudr formations) overlain by a mixed carbonate–mudstone sequence of Palaeocene to Eocene age (Esna, Thebes, Darat, Thal, Tanka and Khaboba formations). The pre-rift units are unconformably overlain by a clastic syn-rift succession of Oligo-Miocene age (Garfunkel and Bartov, 1977; Patton et al., 1994). The syn-rift units form an overall transgressive succession comprising the non-marine Abu Zenima Formation (40–50 m in thickness, age 24–21.5 Ma), the tidally influenced to marginal marine Nukhul Formation (80–100 m in thickness, age 21.5–19.7 Ma), and the open marine Rudeis Formation (19.7–15.5 Ma: ages based on Patton et al., 1994; Krebs et al., 1997). The Abu Zenima and Nukhul formations were deposited during a 'rift initiation' period of relatively slow subsidence rates, while the Rudeis Formation was deposited during a 'rift climax' period of relatively rapid subsidence (Garfunkel and Bartov, 1977; Richardson and Arthur, 1988; Steckler et al., 1988; Patton et al., 1994; Krebs et al., 1997; Gupta et al., 1999). The stratigraphy of the Hammam Faraun fault block, as outlined here, is summarised in Fig. 5.

Six laterally continuous, traceable, key stratigraphic horizons (Horizons A through F) within the syn-rift Nukhul formation have been correlated across the study area based on detailed mapping of the study area (Figs. 4 and 5). These horizons form the basis for geological modelling of the study area, as outlined in Section 4 below.

4. Dataset and methodology

In this study, we integrate data collected through LIDAR (Light Detection and Ranging) based digital outcrop mapping with conventional geological mapping, logging and structural analysis. There are four stages to the workflow; data acquisition, data processing, data interpretation, and modelling (Fig. 5), as summarised below.

4.1. Data acquisition

Data acquisition is based around the use of a terrestrial LIDAR scanner (Bellian et al., 2005; Pringle et al., 2006; Redfern et al., 2007). The instrument used in this study was a Riegl LMS-Z420i scanner (Fig. 6a). The scanner uses a laser to scan the outcrop, returning a series of points, each with x, y and z spatial coordinates and a value for reflection intensity. The resulting series of points is essentially a high-resolution digital elevation model of the outcrop, and is referred to as a point cloud (Fig. 6b). The scanner has a nominal accuracy of 5 mm and scans are collected with an approximate point spacing of 5–10 cm (the scanner operates in terms of angular resolution so the point spacing will vary with the distance between scanner and target). For geo-referencing purposes, a sub-metre accuracy differential GPS (DGPS) reading is taken from the scan position, using a receiver mounted on top of the scanner (Fig. 6a). High-resolution digital images are also collected using a calibrated digital camera mounted on top of the scanner (Fig. 6a), and are used to assign RGB values to the points in the point cloud dataset. The Nukhul half-graben dataset covers an area of approximately 8 km^2, comprises 85 geo-referenced survey positions (Fig. 6c), and includes over 4 billion data points and more than 5000 digital photographs.

4.2. Data processing

Following data collection, InnovMetric's Polyworks® software is used to align the scan data: in this process, overlapping LIDAR scans that were collected from different scan stations are placed in their correct relative positions. This fills in shadow zones that occur in individual scans because they are collected with a single point of view. DGPS positions are then assigned to the scan stations, creating a seamless 3D geo-referenced dataset.

4.3. Data interpretation

Key stratigraphic surfaces (Fig. 5) are mapped across the study area by tracing them on LIDAR-derived point clouds (Fig. 6b). In-house software for geological interpretation of LIDAR data (Virtual Reality Geological Studio – VRGS) is used to tie fault and bedding orientation measurements to the LIDAR dataset. This can be done either through GPS positions for data collected in the field, or by direct measurement from the point cloud data in VRGS. Over 1000 bedding orientation measurements have been derived from the Nukhul LIDAR dataset.

4.4. Modelling

VRGS incorporates a new surface modelling approach that has been developed to overcome the problems associated with outcrop datasets, where there are typically areas of high data density and areas of low to non-existent data density. The new approach is based on triangulated irregular networks (TINs), and is designed to honour both the interpreted key surface traces and the structural data (bedding and fault orientations). A Delaunay-style triangulation (a triangulation method that maximizes the minimum angle within triangles in the resulting mesh, avoiding "sliver" triangles – Delaunay, 1934) is used to create a surface mesh from the input data. Each node of the mesh is associated with information on the elevation of the surface at the node, the dip and strike of the surface at the node, or both. Those nodes that have elevation information are locked in position, while those that only have dip information are moveable. The algorithm calculates the correct orientation of each triangle in the TIN based on the average of the surface orientation at each node, and the triangle is re-oriented into the position around its centroid. This process is applied to each triangle in the mesh in turn. Because moving a triangle will affect the positions of all triangles that share nodes in common, the process is run iteratively until the average z value change of all the nodes at each iteration has fallen below a threshold (typically a very small value, on the order of 0.001 m). In areas close to the edge of the

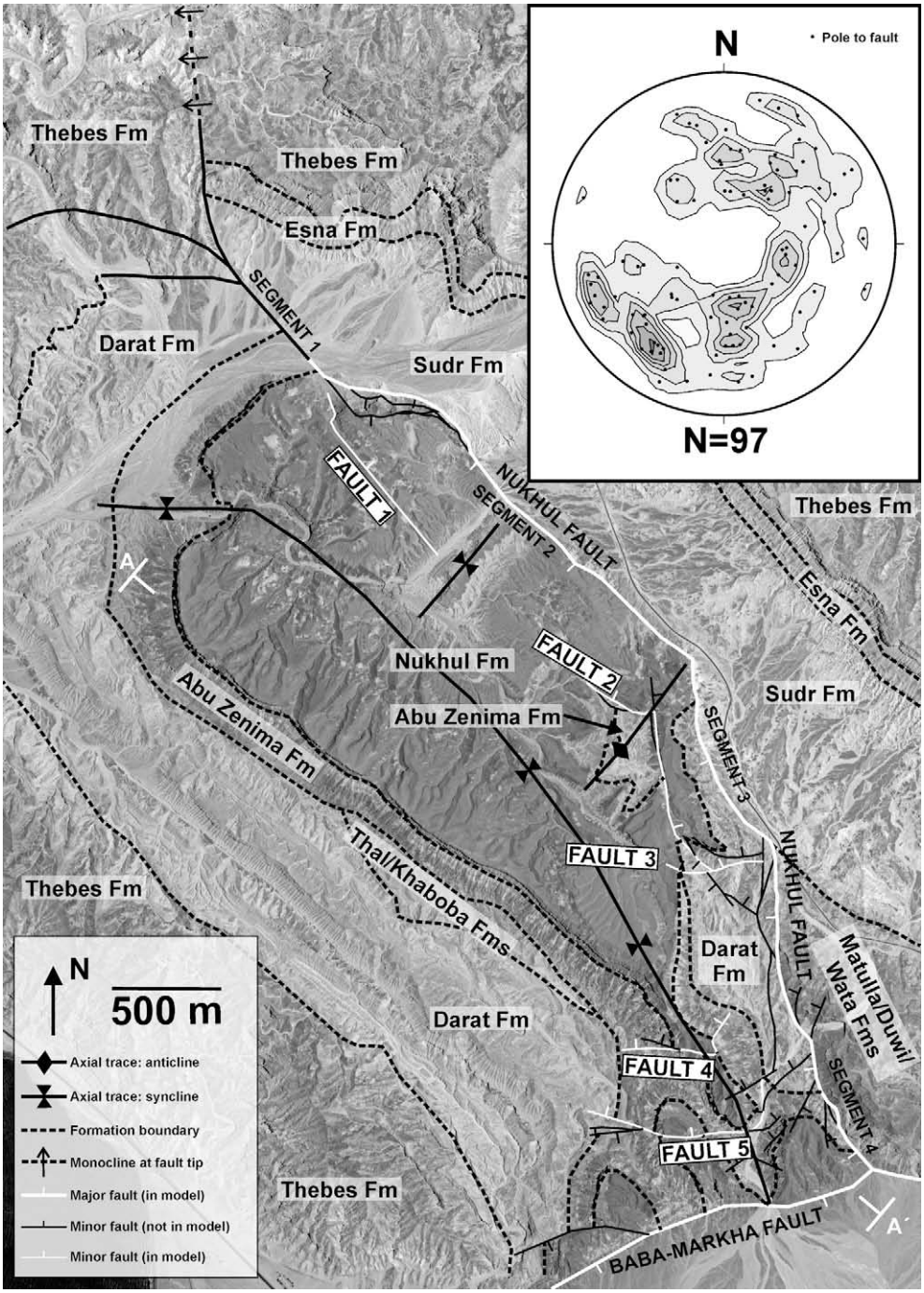

Fig. 4. Simplified geological map of the Nukhul half-graben, showing the structures described in the text. The stereonet at top right shows the orientations of poles to fault planes from the study area.

model, or where data are sparse, triangles may be too large to adequately match the structure of the surface. In this case the grid is refined by inserting nodes until no triangles exist that are greater in size (specified by a maximum edge length: in this case 100 m) than a user-defined threshold value. These inserted nodes have neither a known surface position nor an orientation. For these nodes the dip and azimuth is interpolated from known data.

Once the iterative process is complete, a second phase of mesh refinement around faults is applied (reducing triangle sizes to less than 100 m), and any triangles that cross-faults are removed from the mesh. The mesh is then re-converged to give the final surface which honours faults, structural control and the observed positions of the surface. Manual editing can be used to introduce new control points, edit fault displacements in areas of low data density or add and remove triangles as necessary. The positions of the control nodes can then be used to improve surface gridding in other software packages. An example showing the input data from Horizon E (Fig. 5) is shown in Fig. 7, with the resulting surface shown in Fig. 8a.

In seismic interpretation, squash plots allow lateral variations of thickness and changing stratal geometries on a large scale to be observed by vertically exaggerating seismic profiles. In 3D LIDAR datasets there is an extra level of complexity as the data does not lie in a single plane as it does in seismic data. This problem is

addressed in VRGS by defining a projection plane onto which all data points within a cut-off distance of that plane are projected. The orientation of the plane is user-defined, and the projection direction is normal to the plane. The points are projected down dip onto the planes and added to a bitmap image with defined *X* and *Y* pixel dimensions. The resulting image is a true stratigraphic thickness plot. A squash plot for the West Face of the Nukhul syncline is shown in Fig. 8b.

In the Nukhul study, horizons A, E and F (Fig. 5) were chosen as reference horizons because they are widely exposed and easily recognisable in the study area. The reference horizons were modelled using the surface-building algorithm in VRGS, and exported to Schlumberger's Petrel suite, allowing the intervening horizons to be built with the "Make Zones" process, using isochores calculated between the intervening horizon data and the reference horizons.

Faults were mapped in the field onto high-resolution (pixel size 60 cm) Quickbird satellite images. Fault orientations were measured in the field and additional measurements were derived directly from the LIDAR dataset using VRGS software. A fault model based on these data was built using the interactive fault modelling process in Schlumberger's Petrel suite, and formed the basis of a structural model incorporating the mapped key horizons. Some simplification of the fault geometries was required during the modelling process. Fig. 4 shows the faults mapped in the study area, with those represented by white lines being incorporated into the structural model. Measurements of fault throw were obtained by creating footwall and hangingwall cut-offs in Badley Geoscience Ltd.'s TrapTester software. To exclude problems with data points appearing on the 'wrong' side of the fault and mitigate errors created by fault drag close to fault planes, data points within 10 m (the trim distance) of the fault planes were not used. The cut-offs were calculated using data between 10 and 60 m from the fault planes (i.e. a fault patch width of 50 m in TrapTester). The computer-generated cut-offs were then checked against the horizon and fault data, and edited manually as necessary. In the case of the Nukhul fault, syn-rift strata are not preserved in the footwall (Figs. 3 and 4). However, an estimate of present-day throw was made using the top of the pre-rift Darat Formation as a marker (Fig. 10).

Errors in the throw measurements are derived from uncertainties in horizon picking and uncertainties introduced during the model-building process. Because of the use of very accurate geo-referenced LIDAR data, errors in horizon picks are expected to be significantly less than 1 m. Uncertainties in the model will be very low in areas where data density is high and the model is well constrained, but higher in areas of little or no data. Using the surface-building algorithm in VRGS, structural measurements are used to constrain the model where the key horizons themselves are not exposed. Compared with the use of seismic data (e.g. Nicol et al., 2005; Bull et al., 2006), some significant sources of error are not present (e.g. errors in depth conversion of seismic data) or are significantly reduced (errors in horizon picks resulting from limited

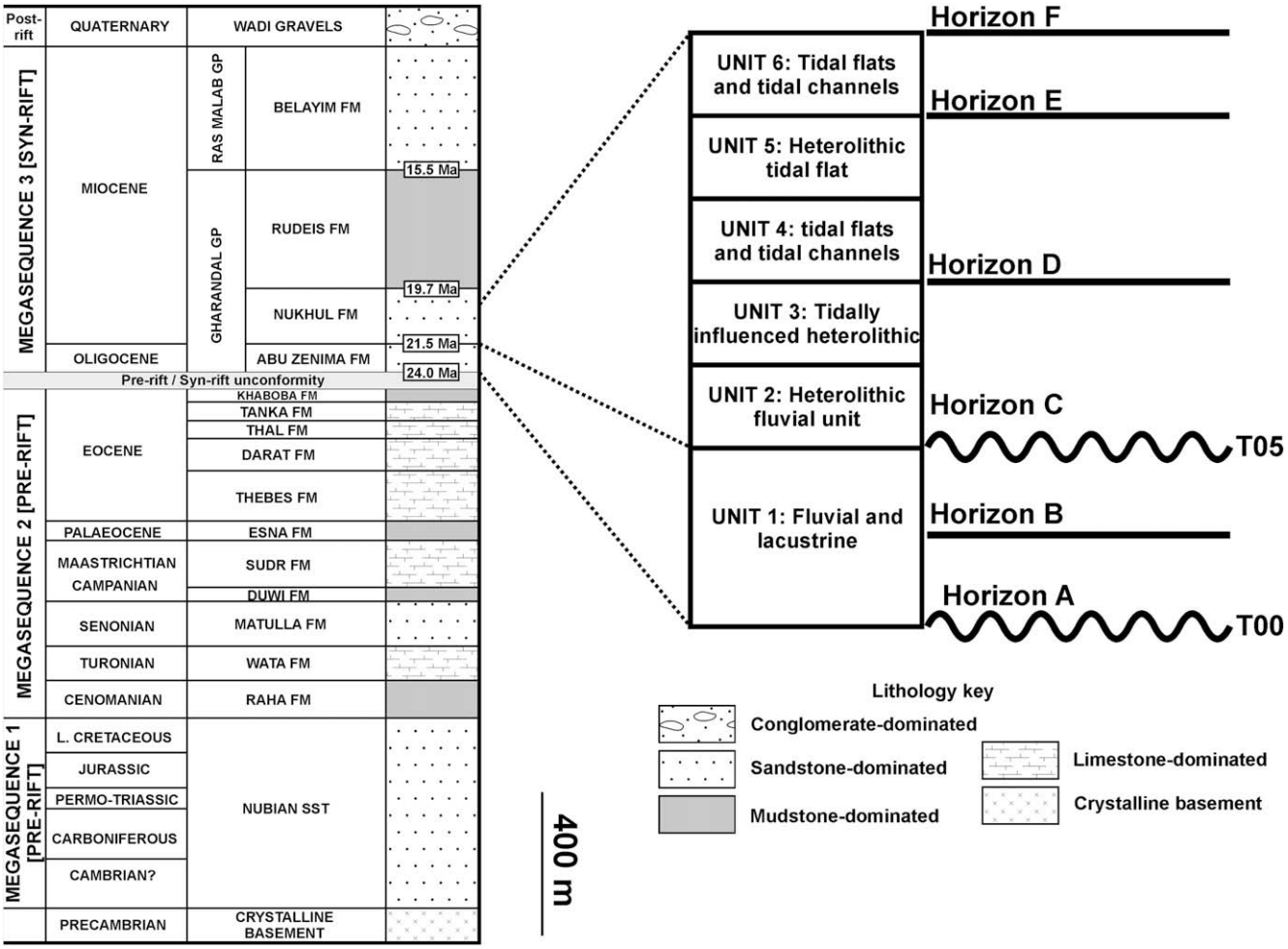

Fig. 5. Stratigraphy of the southern Hammam Faraun fault block, with detailed stratigraphy of the syn-rift succession in the Nukhul half-graben showing the key horizons that have been mapped using LIDAR data. Modified after Jackson et al. (2006).

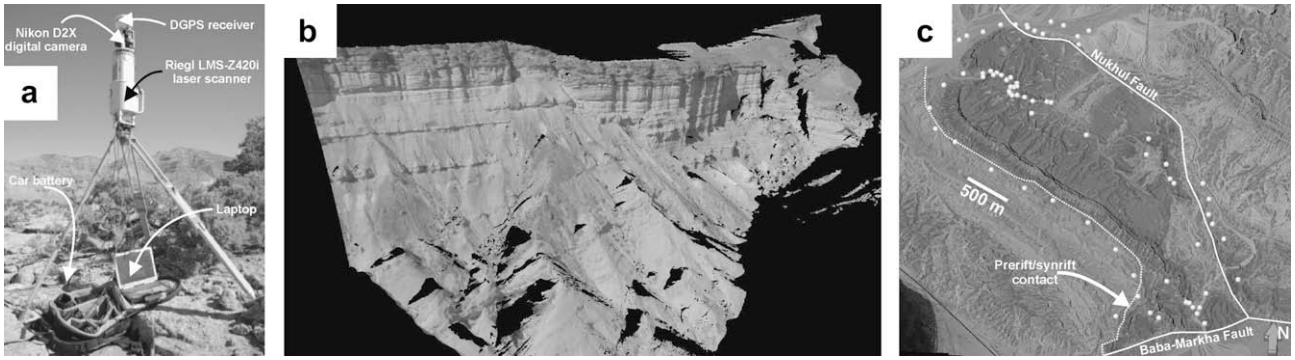

Fig. 6. LIDAR data and data collection. (a) Instrumental set-up for LIDAR data collection. (b) Coloured LIDAR point cloud from the Nukhul half-graben dataset. (c) LIDAR-derived digital elevation model (resolution 1 m) draped with a Quickbird satellite image (resolution 60 cm), showing the positions of the LIDAR scan stations from which data was collected during this study.

resolution of seismic data). Thus we estimate that the maximum error on throw measurements compares favourably with the estimated errors in throw magnitude of 15% estimated by Bull et al. (2006), and is probably on the order of 5–10%.

5. Structural geology of the Nukhul half-graben

The Nukhul fault controlled syn-rift deposition in the Nukhul half-graben (e.g. Sharp et al., 2000a,b; Gawthorpe et al., 2003). The fault dips steeply (50–75°) to the west or southwest. Throw along the fault has been calculated from a LIDAR-derived surface model of the top of the pre-rift Darat Formation (Fig. 10). The maximum throw is approximately 1000 m at the intersection with the Baba–Markha fault in the south, and decreases northwards, over approximately 7.5 km, to a well-defined tip zone and associated fault-tip monocline (Moustafa and Abdeen, 1992; Sharp et al., 2000a,b; Gawthorpe et al., 2003; Figs. 3 and 4). In map view, four segments of the fault can be identified, separated from each other by kinks in the fault trace (Fig. 4). Segments 1 and 2 strike approximately 135° and are linked by a short fault striking 090° (Fig. 4). Segments 3 and 4 strike approximately 155° and are linked by a short fault striking 135° (Fig. 4). Along segments 1 through 3, the syn-rift Abu Zenima and Nukhul formations in the hangingwall are juxtaposed against the pre-rift Sudr Formation in the footwall (Fig. 4). Along segment 4, the pre-rift Darat Formation in the hangingwall is juxtaposed against the pre-rift Matulla, Duwi and Wata formations in the footwall (Fig. 4).

Structure contour maps of key stratigraphic surfaces within the syn-rift strata reveal fault-related folds in the hangingwall of the Nukhul fault (Fig. 9a and b). The most prominent folds are fault-parallel; a syncline developed in the hangingwall of the Nukhul fault and an anticline developed in the footwall of the Baba–Markha fault. Interference between these two folds creates a saddle structure in the south of the study area (Fig. 9a and b). The geometry of folding associated with the Baba–Markha fault can be observed in more detail when LIDAR data from the west face of the Nukhul half-graben is projected into a plane and a vertical exaggeration applied (Fig. 8b). A subtle anticline is observed which is not directly visible from map data or in the field (Fig. 8). The anticline is interpreted to be related to the Baba–Markha fault, as seen at the southern end of Fig. 8b.

The hangingwall syncline parallel to the Nukhul fault is slightly asymmetric, with dips on the eastern limb (5–10°) slightly less than those to the west (10–20°). The trend of the axial trace is approximately NW-SE, sub-parallel to the strike of the Nukhul fault, and the axial trace is approximately 650 m southwest of the trace of the fault at surface. Several folds that are perpendicular to the Nukhul fault are also resolved (Fig. 9a and b). The fault-perpendicular folds have wavelengths varying from approximately 700 m to approximately 1.6 km, and amplitudes varying from approximately 20 m to approximately 120 m. The folds are upright and symmetric, with dips in both limbs approximately 10°. Fault-perpendicular anticlines plunge approximately 10° away from the Nukhul fault, while fault-perpendicular synclines are sub-horizontal. The axes of the fault-perpendicular anticlines correspond roughly to the kinks in the trace of the Nukhul fault that delineate separate fault segments (Figs. 4, 9a and 9b).

Comparing the structure contour maps of the pre-rift/syn-rift contact (base Abu Zenima Formation: Fig. 9a) with the structure contour map for surface ETD within the Nukhul Formation (Fig. 9b), the fault-parallel monocline associated with the Nukhul fault is less pronounced at the higher structural level. This change in structural style occurs abruptly at horizon C (T05), which is locally an angular unconformity in the Nukhul half-graben (Sharp et al., 2000b). It is also clear that the fault-related folding is much less pronounced at the Nukhul level, as would be expected for syn-rift growth folds. Isopach maps for representative intervals within the syn-rift strata show that the Abu Zenima Formation thins dramatically toward the Nukhul fault, while the Nukhul Formation does not display similar thinning (Fig. 9c and d). These data support previous interpretations that the Abu Zenima Formation was deposited in a monoclinal flexure ahead of the still-buried tip of the Nukhul fault, while the Nukhul Formation was deposited following the breaching of the surface by the Nukhul fault (Sharp et al., 2000b; Gawthorpe et al., 2003). The isopach map for the Abu Zenima Formation shows thinning associated with the anticlinal fold that parallels the Baba–Markha fault (Fig. 9c). This suggests that the anticline was present by the time of erosion at the T05 unconformity, indicating that the Baba–Markha fault was active (although possibly still buried) at this time. Fault-perpendicular folds along the Nukhul fault appear to have little influence on the thickness distribution of the Abu Zenima Formation (Fig. 9c). In contrast, the Nukhul formation shows a distinct thin over the fault-perpendicular anticline that occurs at the linkage point between segments 2 and 3 of the Nukhul fault (Fig. 9d), indicating that the presence of the fault-perpendicular anticline is influencing sedimentation patterns in the half-graben.

6. Displacement patterns of faults

Fig. 10 shows variations in throw of the top of the pre-rift Darat Formation along strike of the Nukhul fault. Fig. 11 shows length/throw plots for minor faults 1 through 5 (Fig. 4 for locations), while Fig. 12 shows the minor fault planes contoured for throw magnitude using TrapTester.

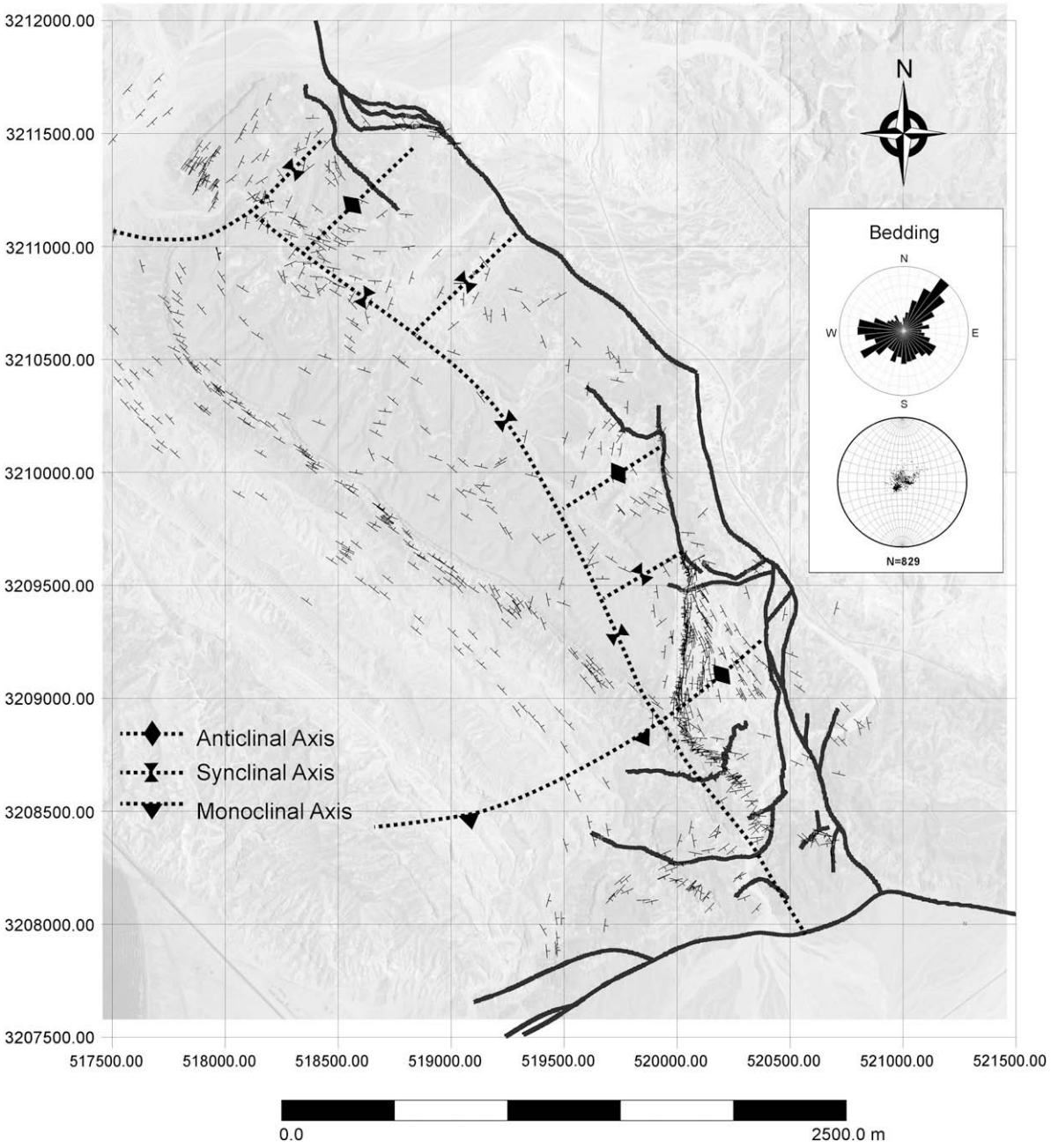

Fig. 7. Map showing the Nukhul half-graben study area, with structural data that were used in the VRGS surface-building algorithm to create the structure contour map shown in Fig. 8.

6.1. The Nukhul fault

Syn-rift strata are not preserved in the footwall of the Nukhul fault, so variations in displacement through time cannot be quantified. However, along-strike variations in throw at the present day can be quantified using pre-rift surfaces as markers. A length/throw profile of the top of the Darat Formation for the Nukhul fault (Fig. 10) shows that the maximum throw is approximately 1000 m where the fault intersects the Baba–Markha fault, consistent with previous estimates (Moustafa and Abdeen, 1992; Gawthorpe et al., 2003). Throw decreases rapidly along segment 4 to the north, until there is a sharp increase where the Nukhul fault intersects Fault 3, at the linkage point between segments 3 and 4 of the Nukhul fault (Figs. 4 and 10). Fault 3 is interpreted as a hangingwall release fault partly accommodating the difference in throw between segments 3 and 4 (Destro, 1995; Destro et al., 2003). Variations in throw corresponding to the positions of fault-perpendicular folds are seen along segments 2 and 3, with throw minima associated with fault-perpendicular anticlines that occur at the linkage points between segments 1 and 2, and segments 2 and 3. Throw is then distributed onto several minor faults with total displacement on the order of 50 m into the tip zone, as displacement is relayed onto a normal fault antithetic to the Nukhul fault in the northwest (Fig. 3).

6.2. Fault 1

Fault 1 is an antithetic structure exposed approximately 300 m into the hangingwall of the Nukhul fault (Fig. 4).

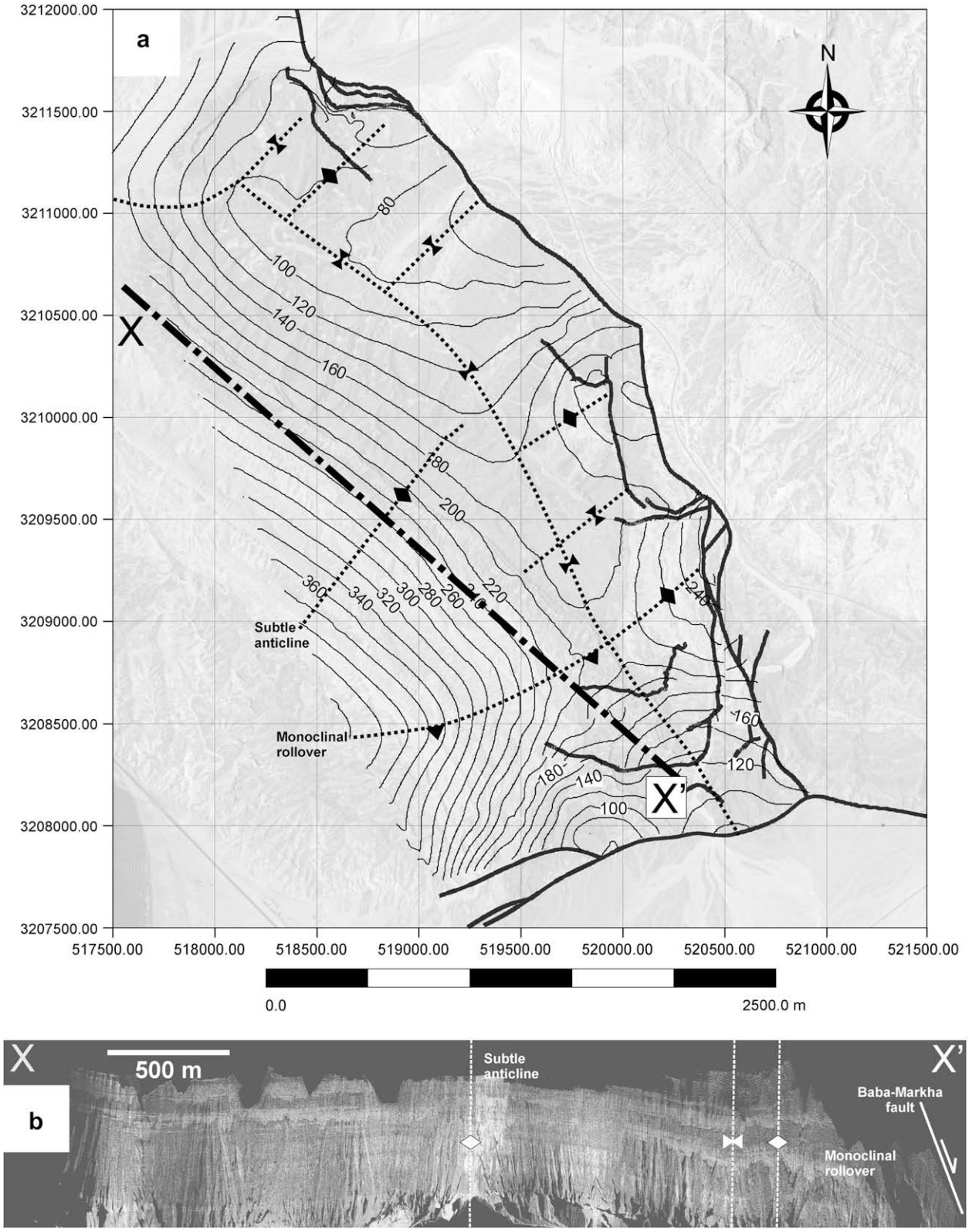

Fig. 8. Structural modelling of the Nukhul half-graben. (a) Structure contour map of horizon E created from the structural data shown in Fig. 7, using the VRGS surface-building algorithm. (b) Squash plot of the LIDAR data from the west face of the Nukhul half-graben (see Fig. 2), showing the presence of subtle folds.

Maximum displacement is approximately 35 m on horizon E (Fig. 11). At horizon F, throw is concentrated near the central portion of the fault, and approaches zero towards the fault tips. Fig. 12a shows that the fault has an elliptical throw high around the centre of the fault plane, and throw decreases radially away from the high. There is also relatively high throw just above the base syn-rift horizon (Horizon A) near the southern end of the fault.

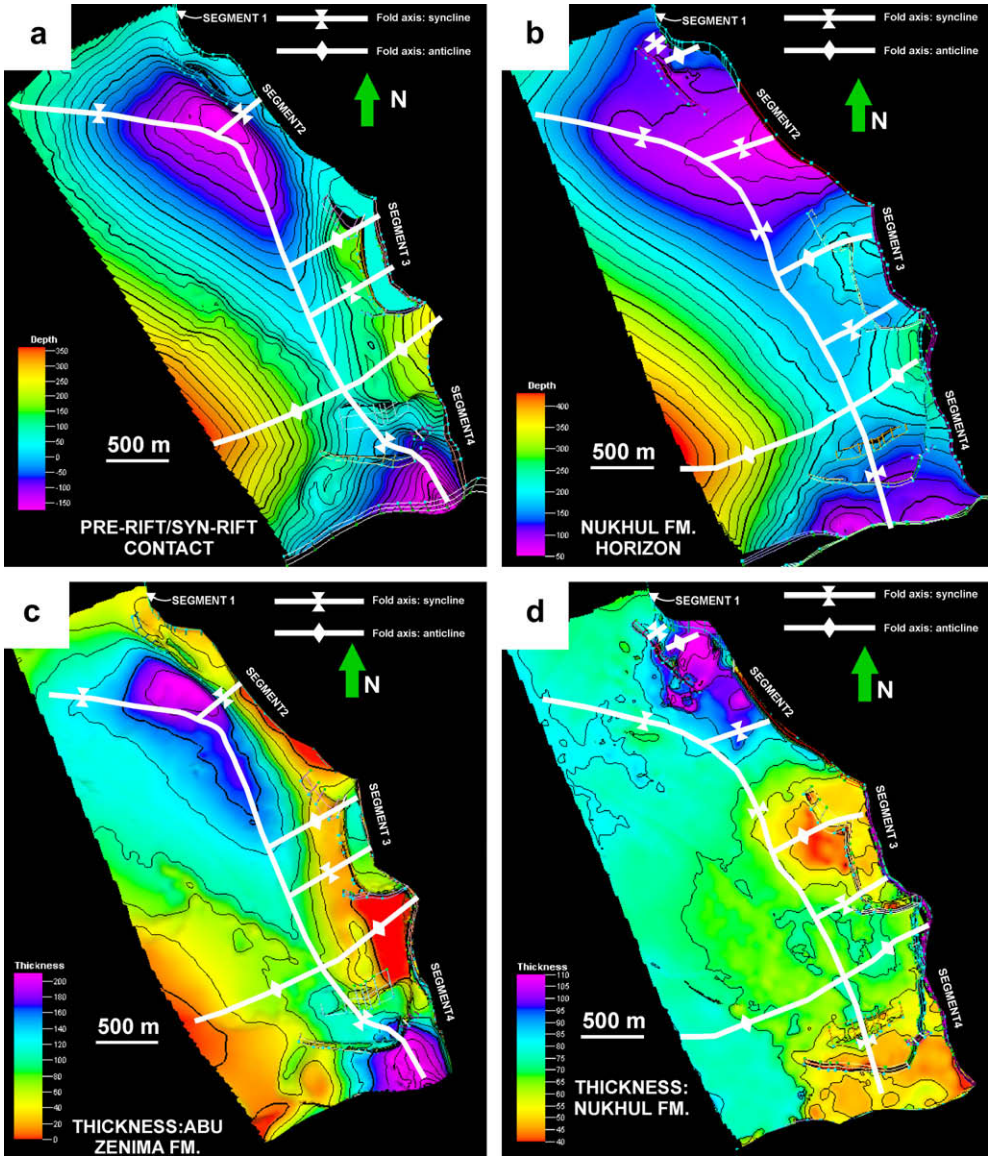

Fig. 9. Structure contour maps and isopach maps for syn-rift strata in the Nukhul half-graben. (a) The base syn-rift horizon. (b) Horizon E within the Nukhul Formation. Isopach maps for (c) the Abu Zenima Formation , horizons A–C; (d) the Nukhul Formation, between horizons C and F.

6.3. Fault 2

Fault 2 forms a linked fault system antithetic to the Nukhul fault, with a strong kink in its trace approximately 300 m into the Nukhul fault hangingwall from the linkage point of Nukhul fault segments 2 and 3 (Fig. 4). The fault shows a maximum throw of a little over 100 m at the base syn-rift horizon (Horizon A), and shows a pattern of decreasing throw with decreasing horizon age (Fig. 11). The throw contours for Fault 2 (Fig. 12b) show an elliptical throw maximum along the more northerly striking segment of the fault, with throw decreasing rapidly upward.

6.4. Fault 3

Fault 3 is an east-striking fault that, at its eastern end, is geometrically linked to segment 3 of the Nukhul fault, and is also linked to Fault 2 (Fig. 4). The length/throw profiles for the fault show that there is a sharp decrease in throw to the west of the linkage point with Fault 3 (Figs. 4 and 11). Between the two linkage points, the maximum displacement increases with increasing horizon age. West of the point where Fault 3 links with Fault 2, throw drops off rapidly towards the fault tip for all horizons (Fig. 11). The throw contour map of the fault shows similar relationships, with throw relatively low west of the linkage point with Fault 2 (Fig. 12c). Maximum throw of approximately 150 m occurs at the linkage point with the Nukhul fault. This pattern of maximum displacement at the intersection point with a major fault, with displacement falling off rapidly into the hangingwall of the major fault, is consistent with the fault being a hangingwall release fault (Destro, 1995; Destro et al., 2003) that formed at the tip of segment 3 of the Nukhul fault prior to the linkage of segments 3 and 4.

Field relationships support the data from fault modelling. In Fig. 13, it can be seen that in the footwall of Fault 3, strata of the pre-rift Darat and syn-rift Abu Zenima formations dip 30–40° to the west and are progressively truncated to the north by an angular unconformity at Horizon C (T05). In the hangingwall of the fault, in contrast, dips both above and below the unconformity are sub-parallel, and

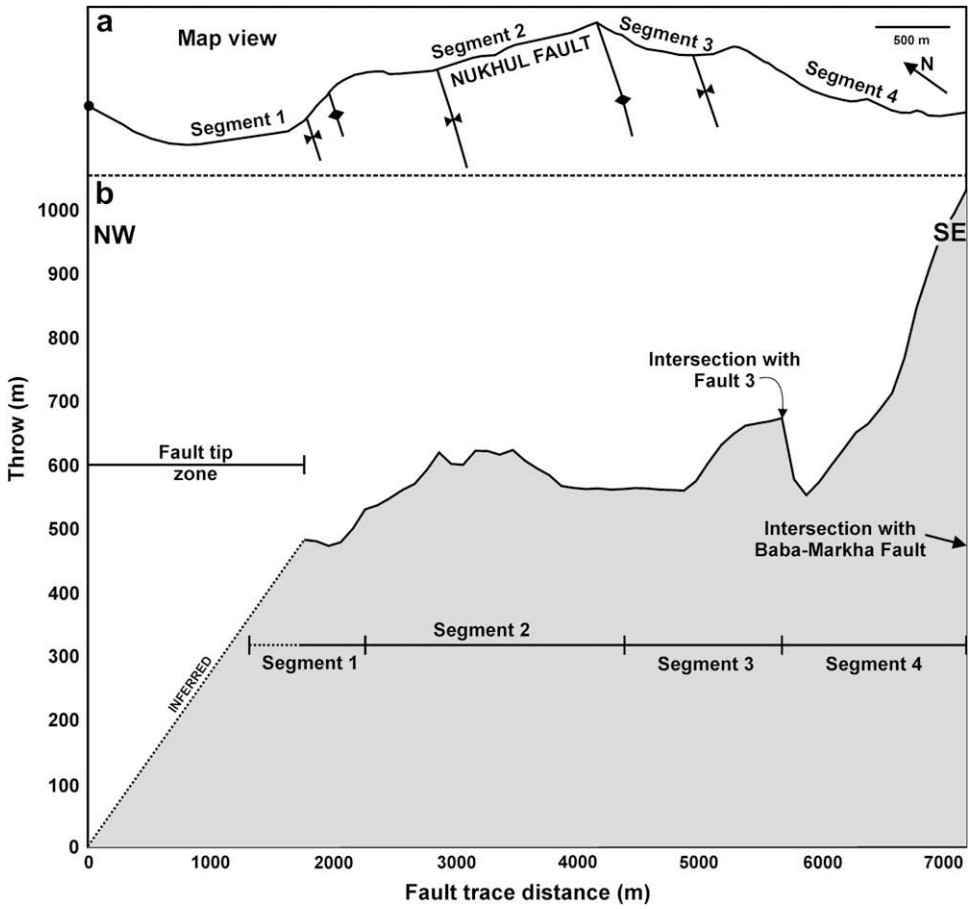

Fig. 10. Length/throw profile of the top of the pre-rift Darat Formation for the Nukhul fault. Maximum throw is approximately 1000 m along segment 4 at the intersection with the Baba–Markha fault. Throw increases rapidly at the intersection with Fault 4. Variations in throw to the north correspond to the positions of fault-perpendicular folds.

surfaces below the unconformity that are truncated in the footwall are preserved (Fig. 13). Projections of stratal surfaces below horizon C onto the fault plane indicate a throw of approximately 80 m. In comparison, the throw of strata in the overlying Nukhul Formation is approximately 12 m.

6.5. Fault 4

Fault 4 is a low-angle, east-striking fault exposed approximately 900 m into the footwall of the Baba–Markha fault (Fig. 4). Throw on horizon A (base syn-rift) and horizon B is relatively low (5 m or less), while throw on the Nukhul Formation horizons is up to approximately 20 m, falling to zero at the fault tips (Fig. 11). The throw contour map for the fault shows a distinct elliptical throw maximum at Nukhul Formation level in the centre of the fault, with throw decreasing away from the maximum (Fig. 12d). Field relationships support these data, with field mapping (Fig. 3) showing that the fault loses displacement downward into pre-rift units.

6.6. Fault 5

Fault 5 is an east-striking fault that outcrops approximately 400 m into the footwall of the Baba–Markha fault (Fig. 4). The length/throw profile shows that the fault is segmented, with throw minima on horizon C (T05) and higher horizons occurring approximately 600 m (L on Fig. 11) from the eastern end of the fault. Throw on horizons A and B is relatively low, in general less than 10 m (Fig. 11). Displacement does not fall to zero at the eastern end of the fault because the fault links with an approximately north-striking fault synthetic to the Nukhul fault, rather than tipping out (Fig. 4). The throw contour map also illustrates the segmented nature of the fault (Fig. 12e). Two throw maxima are observed, one near the eastern end of the fault (maximum displacement 40 m) and one near the western end of the fault (maximum displacement 30 m). Between the two highs displacement drops off to around 10–15 m.

7. Evolution of the Nukhul half-graben

The presence of fault-perpendicular folds in rift basins has been explained through along-strike linkage of previously isolated fault segments as the fault segments grow laterally (Schlische, 1995; Janecke et al., 1998; Sharp et al., 2000a; Jackson et al., 2002; Young et al., 2003). The site of segment linkage represents a displacement minimum on the linked fault system (i.e. the position of a palaeo-fault tip), leading to anticlinal folds with axes perpendicular to the fault at the linkage points between fault segments. Displacement maxima occur at the centre of the fault segments, and are marked by fault-perpendicular synclines. In the Nukhul half-graben, fault-perpendicular folds in the hangingwall of the Nukhul fault (Fig. 9a and b) can be correlated with throw variations along the fault (Fig. 10). Fault-perpendicular anticlines correspond to throw minima, while fault-perpendicular synclines correspond to throw maxima. Hence our conventional and digital outcrop data show that the Nukhul fault is made up of segments that were initially isolated, and grew laterally and linked with each other during their evolution.

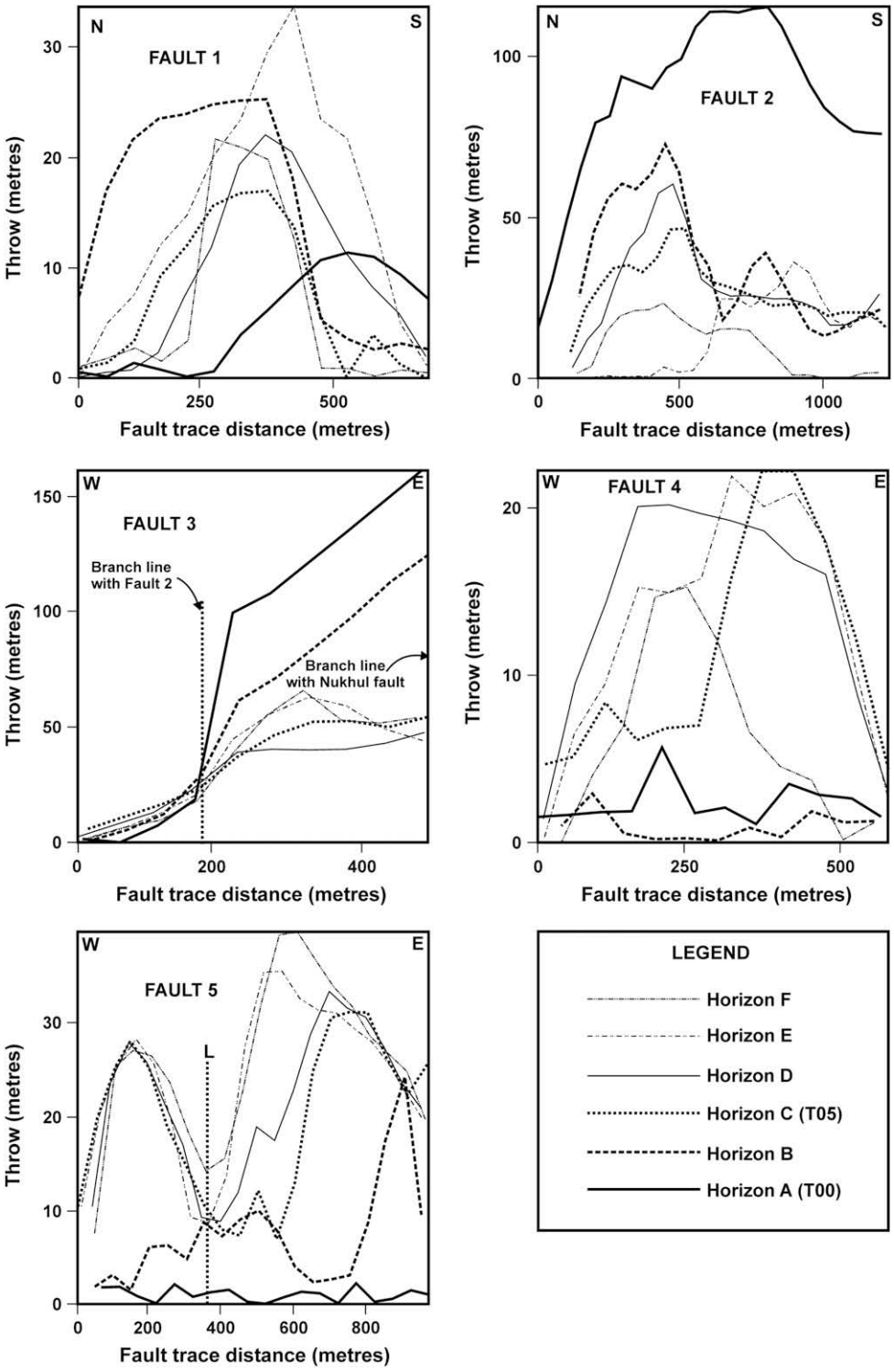

Fig. 11. Length/throw profiles from the TrapTester model of the study area, for faults 1–5 (Fig. 4).

Timing of segment linkage is difficult to determine unequivocally. However, there is evidence to suggest that the segments of the Nukhul fault became linked relatively early in the history of the half-graben. There does not appear to be any systematic variation in the thickness of the Abu Zenima Formation around the fault-perpendicular folds, and there is little evidence for the presence of isolated sub-basins of the type shown in Fig. 1a. Rather, deposition occurred along the entire length of the Nukhul fault for the bulk of the history of activity on the fault. This is supported by the presence of an eroded area where the top 20 m of the Abu Zenima Formation is exposed, associated with the fault-perpendicular anticline at the linkage point between segments 2 and 3 of the Nukhul fault (Figs. 3 and 4). If isolated sub-basins are present, they must be thin, akin to the situation illustrated in Fig. 1b. Also, the sedimentary facies within the Abu Zenima Formation, both in the eroded anticline area (at the linkage point between segments 2 and 3) and in the

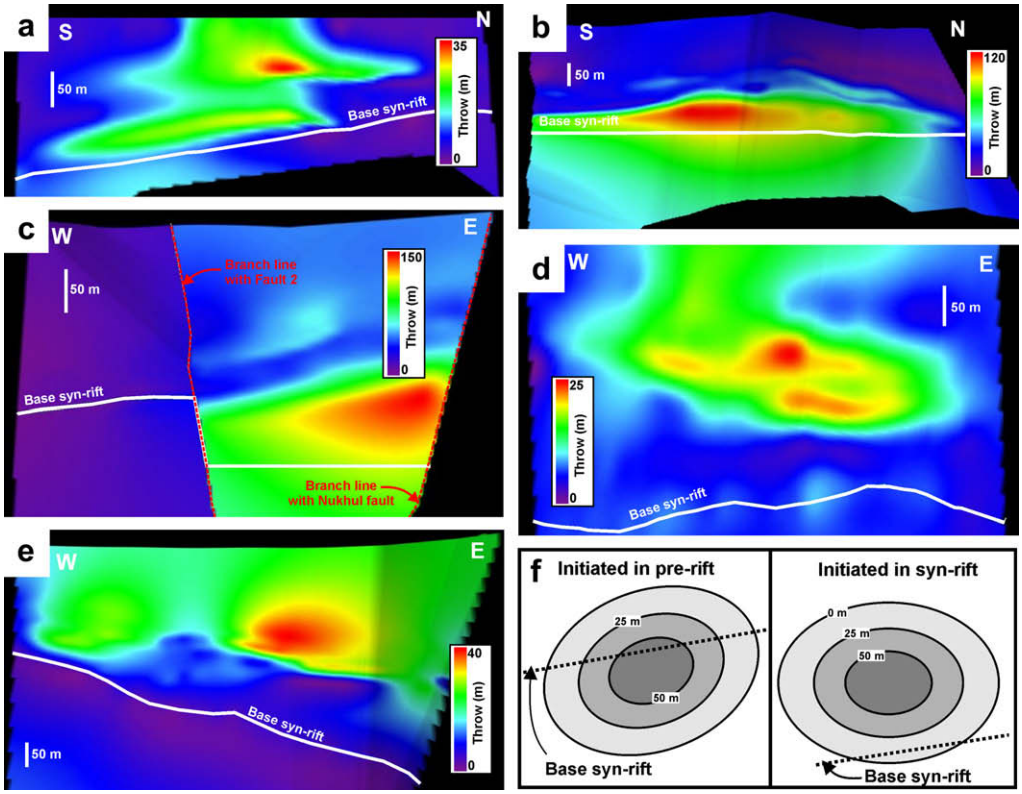

Fig. 12. Fault surfaces contoured for throw magnitude in the TrapTester model of the study area. (a) Fault 1. (b) Fault 2. (c) Fault 3. (d) Fault 4. (e) Fault 5. (f) Schematic throw patterns for isolated faults depending on whether they initiated in the pre-rift or syn-rift strata. (f) Modified after Morley et al. (2007).

northeast of the study area (at the linkage point between segments 1 and 2), is coarser-grained than elsewhere. In the Nukhul Formation, there is no similar change in facies. This suggests that there were sediment input points (possibly relay ramps) at these localities during Abu Zenima time, but not during Nukhul time. Finally, most of the activity on Fault 3 (interpreted as a release fault at the end of segment 3; Fig. 13) occurred in Abu Zenima time, prior to the local unconformity at Surface C (T05). Activity on this fault may relate to the linkage of segments 2 and 3 and consequent subsidence of the anticline area immediately to the north. Taken together, these observations suggest that linkage of fault segments occurred during, or perhaps shortly after, the hiatus represented by the T05 unconformity. Thus linkage occurred by, or shortly after, 21.5 Ma (the age of the T05 unconformity: Patton et al., 1994; Krebs et al., 1997), within the first 2.5 m.y. of rifting.

Throw variations along the Nukhul fault associated with the precursor fault segments persist for at least 1.8 m.y., and perhaps as much as 3.0 m.y., following the linkage of the segments. This is evidenced by the presence of fault-perpendicular folds in the highest preserved units of the Nukhul Formation in the hangingwall of the Nukhul fault (Fig. 4). This is contrary to the conclusion of some previous workers that such structures are unlikely to persist after significant further fault growth (e.g. Anders and Schlische, 1994; Nicol et al., 1996). However, other examples of displacement minima being preserved following linkage have been reported (Rowan et al., 1998; Morley and Wonganan, 2000; McLeod et al., 2000; Nicol et al., 2005). There are at least three possible reasons for preservation of along-strike throw variations in post-linkage strata. Firstly, immaturity of the fault system (i.e. the fault dies before equilibration of displacement can take place; McLeod et al., 2000; Morley and Wonganan, 2000; Gawthorpe et al., 2003). Secondly, that the linked fault does not rupture in its entirety because sharp changes of strike (e.g. 20° between segments 2 and 3 of the Nukhul fault) at segment linkage points impede the propagation of earthquake ruptures (Nicol et al., 2005; Bull et al., 2006). Thirdly, displacement might be geometrically inhibited at fault linkage points where the orientation of the intersection line of the segments is significantly different from the orientation of the slip vector on the fault system (King and Yielding, 1984). The first explanation seems unlikely in this case, as the Nukhul Formation (comprising approximately 60% of the syn-rift fill in the half-graben) was deposited post-linkage. Whether the persistence of displacement lows at the linkage points is related to stopping of earthquake ruptures because of changes in strike, or a geometric effect related to accommodation of displacement along a kinked fault trace cannot be addressed without further data. In either case, however, the preservation of along-strike displacement variations is related to kinks in the fault trace.

Thus our observations support the conclusion that the Nukhul fault attained its present length early in the rift history, and then accrued displacement without significant length change, akin to the development shown in Fig. 1b. However, the Nukhul fault does not fit neatly into either of the end-member fault growth models illustrated in Fig. 1. After fault segment linkage, the displacement history of the fault is still characterised by displacement on independent fault segments (i.e. the fault is *kinematically* segmented, even though it is *geometrically* linked). This leads to displacement minima at fault segment boundaries persisting throughout the displacement history of the fault, as observed for the Nukhul fault. The Nukhul fault is made up of segments of different strike orientations, and we suggest that this pattern of kinematic segmentation following geometric linkage may be typical of faults that consist of segments of different orientations. This is a situation that is likely to be particularly common in rift basins where reactivation of pre-existing structures is important, such as the Suez rift.

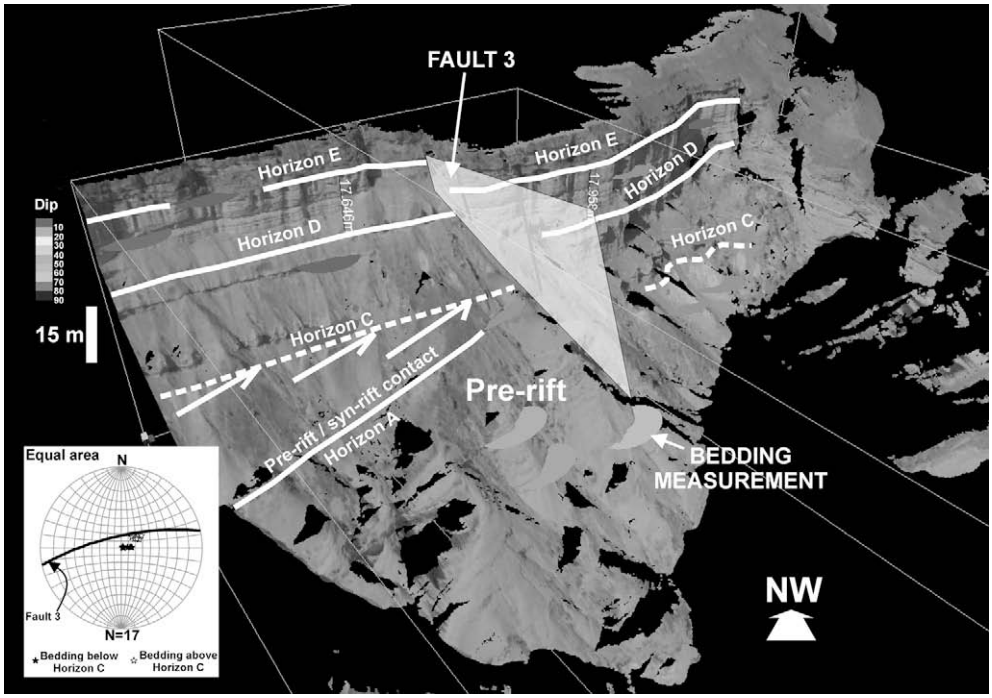

Fig. 13. Interpreted LIDAR point cloud from the east face of the Nukhul half-graben. Note that in the footwall of the approximately east-striking fault that cuts the section here (Fault 3 on Fig. 4), strata below horizon C (T05) are truncated. Strata are not truncated at T05 in the hangingwall of the fault. This is interpreted to reflect erosion of the uplifted footwall block during activity on Fault 3 pre-T05.

Fig. 12f shows the pattern of throw contours in relation to the base syn-rift horizon, depending on whether the faults initiated in pre-rift units or in the syn-rift basin fill (Morley et al., 2007). Assuming that throw contours represent the approximate position of the palaeo-fault-tip line at different stages of propagation, the stratigraphic position of the throw maximum should indicate the age of initiation of the fault (e.g. Morley et al., 2007). From this study, there is evidence that some of the minor faults in the Nukhul half-graben initiated within the syn-rift basin fill, while others initiated below or close to the base syn-rift horizon. Fig. 12b shows throw contours for the Fault 2 (Fig. 4). The maximum throw for this linked fault system occurs just above the base syn-rift horizon. A similar relationship is observed for Fault 3 (Fig. 12c), and is supported by outcrop observations that throw increases significantly downward on Fault 3 (Fig. 13). This suggests that faults 2 and 3 initiated within or just above the pre-rift strata, and propagated upward through the syn-rift strata (and downward through pre-rift strata) with time. In contrast, throw contours (Fig. 12a,d and e) of faults 1, 4 and 5 show that the throw maxima for each of these faults are within the Nukhul Formation, well above the base syn-rift horizon. This suggests that these faults initiated within the syn-rift, and propagated both upward and downward through the syn-rift strata. The presence of a displacement minimum along Fault 5 indicates that the fault developed by linkage of previously isolated segments, showing that lateral propagation of the precursor fault segments was important (Fig. 12e).

Evidence from isopach maps suggests that the Baba–Markha fault was active during Abu Zenima time (Fig. 9c). Nonetheless, cross-cutting relationships between the Baba–Markha fault and the Nukhul fault show that the majority of displacement on the Baba–Markha fault accrued later than that on the Nukhul fault (Gawthorpe et al., 2003). Throw contour maps for east-striking faults (faults 4 and 5; Fig. 12d and e) in the footwall of the Baba–Markha fault show that these faults initiated relatively late in the history of the Nukhul half-graben, during late Nukhul time, when some northwest-striking faults are dying out. Thus within the Nukhul half-graben there is an evolution of fault activity from faults in the hangingwall of the Nukhul fault (Abu Zenima and early Nukhul time), to faults in the footwall of the Baba–Markha fault. We suggest that this evolution may be related to waning activity on the Nukhul fault, and increasing activity (and/or surface breaching) on the Baba–Markha fault. A similar pattern of late 'basin-initiating' faults has been recognised from the Phitsanulok basin of Thailand, where the stress field orientation changed late in the rift history, giving rise to a new fault set (Morley et al., 2007). In the Gulf of Suez, the stress field orientation is thought to have been roughly constant between the initiation of rifting at 24 Ma and the initiation of the Aqaba-Levant transform at 14 Ma (Steckler et al., 1988; Lyberis, 1988; Bosworth et al., 2005) so changes in stress field orientation are unlikely to explain the evolution of fault orientations in the Nukhul half-graben. In any case, the evidence shows that east-striking faults have been active throughout the development of the half-graben. For example, the Baba–Markha fault and Fault 3 were clearly active in pre-Nukhul time (Figs. 9c and 13). We suggest that the evolution from active faults in the hangingwall of the Nukhul fault to active faults in the footwall of the Baba–Markha fault occurred during the transition from rift initiation to rift climax, as strain was increasingly localised onto the present-day block-bounding faults (e.g. the Baba–Markha fault) and the present-day intra-block faults (e.g. the Nukhul fault) began to die out (Gawthorpe et al., 2003).

Numerical modelling and outcrop study has shown that fault growth and linkage leads to a progressive decrease in the number of active faults, with displacement increasingly localised onto a few block-bounding structures (e.g. Cowie et al., 2000; Gawthorpe et al., 2003). Our results show that at the half-graben scale, in complex rifts with several fault orientation sets, this progression may occur at different times for each fault set. In this case there is a transient increase in fault activity in late Nukhul time that is associated with increased activity on the Baba–Markha fault.

Based on the above arguments, the structural evolution of the Nukhul half-graben is summarised in Fig. 14. The Nukhul fault was

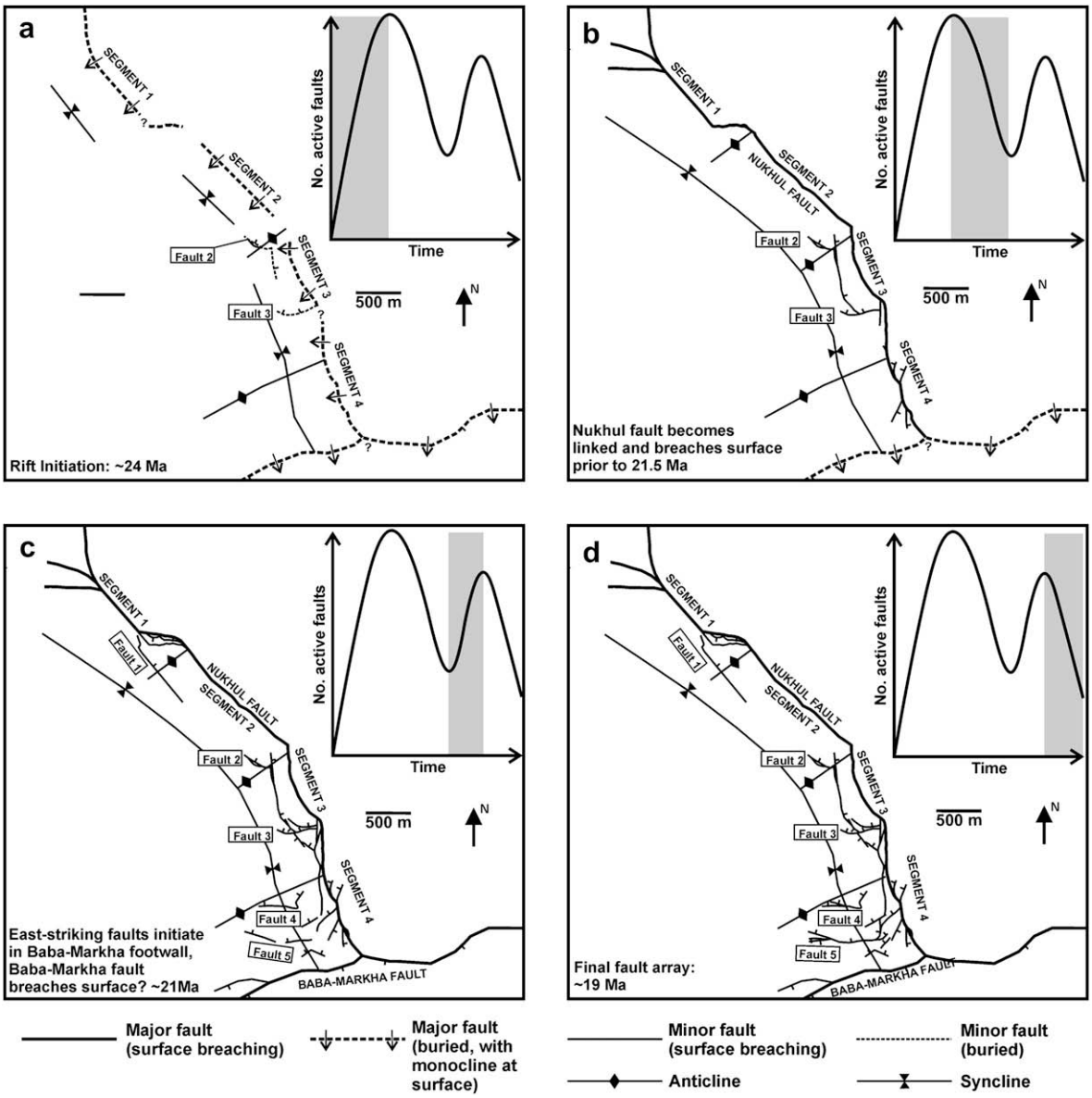

Fig. 14. Evolution of the fault array in the Nukhul half-graben. (a). Rift initiation, ~24 Ma. The Nukhul fault is initially geometrically segmented. Segments 1, 3 and 4 of the Nukhul fault are reactivated structures, with segment 2 initiating during rifting. Fault 3, and possibly Fault 2, are also active at this time. (b) Lateral propagation of segment 2 leads to linkage the Nukhul fault, probably by ~22 Ma. Faults 2 and 3 form a linked system in the hangingwall of the Nukhul fault. (c) Increasing activity on the Baba–Markha fault in late Nukhul time (~20 Ma) is associated with the initiation of antithetic structures within the basin fill in the Baba–Markha fault footwall. Fault 1 also initiates at this time. (d) Antithetic structures in the Baba–Markha fault footwall grow and link to other structures along strike, creating the final fault array as observed at the present day. After this point, displacement is increasingly localised onto the present-day block-bounding structures (the Thal, Hammam Faraun, Baba–Sidri, Nezzazat and Baba–Markha faults: see Fig. 1), leading to the onset of rift-climax rapid subsidence and deposition of the Rudeis Formation (Patton et al., 1994; Gawthorpe et al., 2003). Faults in the Nukhul half-graben become inactive.

initially blind and geometrically segmented. Segments 1, 3 and 4 of the Nukhul fault were reactivated structures, with segment 2 initiating during rifting. Fault 3 was active as a hangingwall release fault (Destro, 1995; Destro et al., 2003), and Fault 2 was also active at this time. Lateral propagation of segment 2 led to linkage the Nukhul fault and vertical propagation led to the Nukhul fault breaching the surface, in both cases probably by ~22 Ma. Faults 2 and 3 formed a linked system in the hangingwall of the Nukhul fault (Fig. 14b). Increasing activity on the Baba–Markha fault in late Nukhul time (~20 Ma) was associated with the initiation of antithetic faults within the basin fill in the Baba–Markha fault footwall; Fault 1 also initiated at this time (Fig. 14c). Antithetic faults in the Baba–Markha fault footwall grew and linked to other faults along strike, creating the final fault array as observed at the present day (Fig. 14d). After that point, displacement was increasingly localised onto the present-day block-bounding faults (the Thal, Hammam Faraun, and Baba–Markha faults: see Fig. 2), leading to the onset of rift-climax rapid subsidence and deposition of the Rudeis Formation (Patton et al., 1994; Gawthorpe et al., 2003), and faults in the Nukhul half-graben become inactive.

8. Conclusions

1. The LIDAR-based digital outcrop mapping methodology used in this study, in conjunction with new surface-building algorithms designed for use with outcrop data, allows us to obtain detailed data on the spatial position of faults and stratigraphic horizons. It is then possible to create accurate tectono-

stratigraphic models of the study area, and gain a quantitative understanding of thickness patterns of syn-rift strata and displacement patterns of faults.

2. The Nukhul fault is segmented. Throw minima occur at the linkage points of the fault segments, suggesting lateral propagation and linkage of initially spatially separate fault segments. The linkage occurred within the first 2.4 m.y. of rifting, showing that the fault system attained its length very early in the history of the Suez rift. Throw minima along the linked fault persisted throughout deposition of at least 80% of the preserved rift-initiation strata (Abu Zenima and Nukhul formations). This suggests that the fault remained kinematically segmented during its post-linkage history.
3. Length/throw patterns and throw contours for faults in the hangingwall of segment 3 of the Nukhul fault (faults 2 and 3) suggest that these faults initiated in early syn-rift time, prior to deposition of the Nukhul Formation. Length/throw patterns and throw contours for faults in the footwall of the Baba–Markha fault (faults 4 and 5), and an antithetic fault in the hangingwall of segment 2 of the Nukhul fault (Fault 1) suggest that these faults initiated later in the rift history, during Nukhul time.
4. The syn-rift development of the Nukhul half-graben is characterised both by structures that initiated within pre-rift units and propagate upward into the syn-rift basin fill, and structures that initiated within the syn-rift megasequence. Both east-striking and north- to northwest-striking faults are active throughout rifting in the Nukhul half-graben, although east-striking faults in the footwall of the Baba–Markha fault dominate later in the history. This may be a result of increasing activity on the Baba–Markha fault, and decreasing activity on the Nukhul fault, into the transition between rift initation and rift climax in late Nukhul time.
5. Rather than a continuous decrease in the number of active faults during rifting, there may be transient highs in the number of active faults as faults initiate and develop in new orientations during rift evolution.

Acknowledgments

This work was funded by the Rift Analogues Project consortium, consisting of Norsk Hydro and Statoil (now merged as StatoilHydro), and ConocoPhilips. Schlumberger provided licenses for Petrel. Badley Geoscience Ltd. provided licenses for TrapTester. We acknowledge reviews by G. Yielding and J. Hippertt. Logistical support in the field was provided by Sayed, Gamal and Bilal Gooda.

References

Anders, M.H., Schlische, R.W., 1994. Overlapping faults, intrabasin highs, and the growth of normal faults. Journal of Geology 102, 165–179.
Bellahsen, N., Daniel, J.M., 2005. Fault reactivation control on normal fault growth: an experimental study. Journal of Structural Geology 27, 769–780.
Bellian, J.A., Kerans, C., Jennette, D.C., 2005. Digital outcrop models: applications of terrestrial scanning LIDAR technology in stratigraphic modeling. Journal of Sedimentary Research 75, 166–176.
Bosworth, W., Huchon, P., McClay, K., 2005. The Red Sea and Gulf of Aden basins. Journal of African Earth Sciences 43, 334–378.
Bull, J.M., Barnes, P.M., Lamarche, G., Sanderson, D.J., Cowie, P.A., Taylor, S.K., Dix, J.K., 2006. High-resolution record of displacement accumulation on an active normal fault: implications for models of slip accumulation during repeated earthquakes. Journal of Structural Geology 28, 1146–1166.
Cartwright, J.A., Trudgill, B.D., Mansfield, C.S., 1995. Fault growth by segment linkage: an explanation for scatter in maximum displacement and trace length data from the Canyonlands Grabens of SE Utah. Journal of Structural Geology 17, 1319–1326.
Contreras, J., Anders, M.H., Scholz, C.H., 2000. Growth of a normal fault system: observations from the Lake Malawi basin of the east African rift. Journal of Structural Geology 22, 159–168.
Corfield, S., Sharp, I.R., 2000. Structural style and stratigraphic architecture of fault propagation folding in extensional settings: a seismic example from the Smørburkk area, Halten Terrace, Mid-Norway. Basin Research 12, 329–341.
Cowie, P.A., Gupta, S., Dawers, N.H., 2000. Implications of fault array evolution for synrift depocentre development: insights from a numerical fault growth model. Basin Research 12, 241–261.
Delaunay, B., 1934. Sur la sphère vide. Izvestia Akademii Nauk SSSR, Otdelenie Matematicheskikh i Estestvennykh Nauk 7, 793–800.
Destro, N., 1995. Release fault: a variety of cross-fault in linked extensional systems, in the Sergipe-Alagoas Basin, NE Brazil. Journal of Structural Geology 17, 615–629.
Destro, N., Szatmari, P., Alkmim, F.F., Magnavita, L.P., 2003. Release faults, associated structures, and their control on petroleum trends in the Recôncavo rift, northeast Brazil. AAPG Bulletin 87, 1123–1144.
Garfunkel, Z., Bartov, Y., 1977. The tectonics of the Suez Rift. Geological Survey of Israel Bulletin 71, 1–41.
Gawthorpe, R.L., Leeder, M.R., 2000. Tectono-sedimentary evolution of active extensional basins. Basin Research 12, 195–218.
Gawthorpe, R.L., Jackson, C.A.-L., Young, M.J., Sharp, I.R., Moustafa, A.R., Leppard, C.W., 2003. Normal fault growth, displacement localisation and the evolution of normal fault populations: the Hammam Faraun fault block, Suez rift, Egypt. Journal of Structural Geology 25, 883–895.
Gupta, S., Underhill, J.R., Sharp, I.R., Gawthorpe, R.L., 1999. Role of fault interactions in controlling synrift sediment dispersal patterns; Miocene, Abu Alaqa Group, Suez Rift, Sinai, Egypt. Basin Research 11, 167–189.
Jackson, C.A.L., Gawthorpe, R.L., Sharp, I.R., 2002. Growth and linkage of the East Tanka fault zone, Suez rift: structural style and syn-rift stratigraphic response. Journal of the Geological Society of London 159, 175–187.
Jackson, C.A.L., Gawthorpe, R.L., Sharp, I.R., 2006. Style and sequence of deformation during extensional fault-propagation folding: examples from the Hammam Faraun and El-Qaa fault blocks, Suez Rift, Egypt. Journal of Structural Geology 28, 519–535.
Janecke, S.U., Vandenburg, C.J., Blankenau, J.J., 1998. Geometry, mechanisms and significance of extensional folds from examples in the Rocky Mountain Basin and Range province. U.S.A. Journal of Structural Geology 20, 841–856.
King, G., Yielding, G., 1984. The evolution of a thrust fault system: processes of rupture initiation, propagation and termination in the 1980 El Asnam (Algeria) earthquake. Geophysical Journal International 77, 915–933.
Krebs, W.N., Wescott, W.A., Nummedal, D., Gaafar, I., Azazi, G., Karamat, S., 1997. Graphic correlation and sequence stratigraphy of Neogene rocks in the Gulf of Suez. Bulletin de la Société Géologique de France 168, 63–71.
Lyberis, N., 1988. Tectonic evolution of the Gulf of Suez and Gulf of Aqaba. Tectonophysics 153, 209–220.
Manzocchi, T., Walsh, J.J., Nicol, A., 2006. Displacement accumulation from earthquakes on isolated normal faults. Journal of Structural Geology 28, 1685–1693.
McLeod, A.E., Dawers, N.H., Underhill, J.R., 2000. The propagation and linkage of normal faults: insights from the Strathspey-Brent-Statfjord fault array, northern North Sea. Basin Research 12, 263–284.
Montenat, C., D'Estevou, P.O., Purser, B., Burollet, P.-F., Jarrige, J.-J., Orszag-Sperber, F., Philobbos, E., Plaziat, J.-C., Prat, P., Richert, J.-P., Roussel, N., Thiriet, J.-P., 1988. Tectonic and sedimentary evolution of the Gulf of Suez and the northwestern Red Sea. Tectonophysics 153, 161–177.
Morley, C.K., 1999. How successful are analogue models in addressing the influence of pre-existing fabrics on rift structure? Journal of Structural Geology 21, 1267–1274.
Morley, C.K., 2002. Evolution of large normal faults: Evidence from seismic reflection data. American Association of Petroleum Geologists Bulletin 86, 961–978.
Morley, C.K., Wonganan, N., 2000. Normal fault displacement characteristics, with particular reference to synthetic transfer zones, Mae Moh mine, northern Thailand. Basin Research 12, 307–327.
Morley, C.K., Gabdi, S., Seusutthiya, K., 2007. Fault superimposition and linkage resulting from stress changes during rifting: Examples from 3D seismic data, Phitsanulok Basin, Thailand. Journal of Structural Geology 29, 646–663.
Moustafa, A.R., 1987. Drape folding in the Baba–Sidri area, eastern side of Suez Rift, Egypt. Journal of Geology 31, 15–27.
Moustafa, A.R., 1993. Structural characteristics and tectonic evolution of the east margin blocks of the Suez rift. Tectonophysics 223, 381–399.
Moustafa, A.R., 1996. Internal structure and deformation of an accommodation zone in the northern part of the Suez rift. Journal of Structural Geology 18, 93–107.
Moustafa, A.R., 1997. Controls on the development and evolution of transfer zones: the influence of basement structure and sedimentary thickness in the Suez rift and Red Sea. Journal of Structural Geology 19, 755–768.
Moustafa, A.R., Abdeen, A.R., 1992. Structural setting of the Hammam Faraun fault block, eastern side of the Suez Rift. Journal of the University of Kuweit (Science) 19, 291–310.
Nicol, A., Watterson, J., Walsh, J.J., Childs, C., 1996. The shapes, major axis orientations and displacement patterns of fault surfaces. Journal of Structural Geology 18, 235–248.
Nicol, A., Walsh, J., Berryman, K., Nodder, S., 2005. Growth of a normal fault by the accumulation of slip over millions of years. Journal of Structural Geology 27, 327–342.
Patton, T.L., Moustafa, A.R., Nelson, R.A., Abdine, A.S., 1994. In: Landon, S.M. (Ed.), Interior Rift Basins. Tectonic Evolution and Structural Setting of the Gulf of Suez Rift, 59. American Association of Petroleum Geologists Memoir, pp. 9–55.
Pringle, J.K., Howell, J.A., Hodgetts, D., Westerman, A.R., Hodgson, D.M., 2006. Virtual outcrop models of petroleum reservoir analogues: a review of the current state-of-the-art. First Break 24, 33–42.

Redfern, J., Hodgetts, D., Fabuel-Perez, I., 2007. Digital analysis brings renaissance for petroleum geology outcrop studies in North Africa. First Break 25, 81–87.
Richardson, M., Arthur, M.A., 1988. The Gulf of Suez – northern Red Sea Neogene rift: a quantitative basin analysis. Marine and Petroleum Geology 5, 247–270.
Robson, D.A., 1971. The structure of the Gulf of Suez (Clysmic) Rift, with special reference to the eastern side. Journal of the Geological Society of London 127, 247–271.
Rowan, M.G., Hart, B.S., Nelson, S., Flemings, P.B., Trudgill, B.D., 1998. Three-dimensional geometry and evolution of a salt-related growth-fault array: Eugene Island 330 field, offshore Louisiana, Gulf of Mexico. Marine and Petroleum Geology 15, 309–328.
Schlische, R.W., 1995. Geometry and origin of fault-related folds in extensional basins. American Association of Petroleum Geologists Bulletin 79, 1246–1263.
Sharp, I.R., Gawthorpe, R.L., Underhill, J.R., Gupta, S., 2000a. Fault-propagation folding in extensional settings: examples of structural style and synrift sedimentary response from the Suez rift, Sinai, Egypt. Geological Society of America Bulletin 112, 1877–1899.
Sharp, I.R., Gawthorpe, R.L., Armstrong, B., Underhill, J.R., 2000b. Propagation history and passive rotation of mesoscale normal faults: implications for syn-rift stratigraphic development. Basin Research 12, 285–306.
Steckler, M.J., Berthelot, F., Lyberis, N., LePichon, X., 1988. Subsidence in the Gulf of Suez: implications for rifting and plate kinematics. Tectonophysics 153, 249–270.
Wilson, P., Gawthorpe, R.L., Hodgetts, D., Rarity, F., Sharp, I.R. Geometry and architecture of a half-graben scale syn-rift normal fault array: the Nukhul half-graben, Suez rift, Egypt. Journal of Structural Geology, submitted for publication.
Younes, A.I., McClay, K.R., 2002. Development of accommodation zones in the Gulf of Suez-Red Sea Rift, Egypt. Bulletin of the American Association of Petroleum Geologists 86, 1003–1026.
Young, M.J., Gawthorpe, R.L., Sharp, I.R., 2000. Sedimentology and sequence stratigraphy of a transfer zone coarse-grained delta, Miocene Suez Rift, Egypt. Sedimentology 47, 1081–1104.
Young, M.J., Gawthorpe, R.L., Sharp, I.R., 2003. Normal fault growth and early syn-rift sedimentology and sequence stratigraphy; Thal Fault, Suez Rift, Egypt. Basin Research 15, 479–502.